POLITECNICO DI TORINO
Repository ISTITUZIONALE

Multi-Fidelity Analysis of a Small-Scale Propeller Using VPM Against URANS and Experimental Data

Original
Multi-Fidelity Analysis of a Small-Scale Propeller Using VPM Against URANS and Experimental Data / Grava, A., Serpieri, J., Bernardos, L., Cafiero, G.. - (2025). (AIAA AVIATION FORUM AND ASCEND, 2025 Las Vegas, Nevada (USA) 21 - 25 July 2025) [10.2514/6.2025-3163].

Availability:
This version is available at: 11583/3008348 since: 2026-03-07T15:36:45Z

Publisher:
American Institute of Aeronautics and Astronautics, AIAA

Published
DOI:10.2514/6.2025-3163

Terms of use:

This article is made available under terms and conditions as specified in the corresponding bibliographic description in the repository

Publisher copyright
AIAA preprint/submitted version e/o postprint/Author's Accepted Manuscript

(Article begins on next page)

09 June 2026

Multi-fidelity analysis of a small-scale propeller using VPM against URANS and experimental data

Grava Alessandro *, Serpieri Jacopo †
Polytechnic University of Turin, Corso Duca degli Abruzzi 24, 10129, Turin, Italy

Bernardos Luis‡
DAAA, ONERA, Polytechnic Institute of Paris, 92190, Meudon, France

Cafiero Gioacchino §
Polytechnic University of Turin, Corso Duca degli Abruzzi 24, 10129, Turin, Italy

The recent increase in small drones popularity carries along some critical aspects, especially regarding the evaluation of their aerodynamic performance. Their small-scale propellers operate in challenging fluid dynamics regimes, characterized by complex transitional phenomena which are typical of low chord-based Reynolds numbers. In this work, an isolated small-scale propeller is analyzed with different techniques in hovering and axial inflow. An experimental campaign was initially carried out, evaluating the propeller thrust and torque with dedicated load sensors and the induced velocity in the wake with the planar PIV. Subsequently, the propeller was simulated with the use of the mid-high fidelity URANS methodology through an overset mesh approach. The SST $k-\omega$ turbulence model coupled with the $\gamma - Re_\theta$ transition model was chosen for the purpose, attempting to properly capture the transitional phenomena in the flow. Finally, a further simulation campaign was conducted using the low-fidelity VPM code VULCAINS, in-house-built by ONERA. The code allowed to obtain accurate results at a very reduced computational cost, with the further advantage of being a meshless method, leading to a very straightforward simulations pre-processing. The outcomes of the three methodologies are remarkably similar mostly in axial inflow, showing errors under 4% for both thrust and torque coefficients and under 5% for what instead concerns the axial velocity in the wake. On the other hand, a slight mismatch is present in the hovering condition, featured by errors under 8% on the performance coefficients and around 10% to 15% for the axial velocity. Furthermore, the influence of the most relevant input parameters in the VPM code is investigated. The number of vorticity sources shed from the blades per time-step stands out as the most influential parameter, slightly affecting the time-averaged loads, the induced velocity in the wake and the total computational time.

I. Nomenclature

c	=	blade chord [m]
C_T	=	non-dimensional thrust coefficient, $C_T = \frac{T}{\rho\pi R^2(\Omega R)^2}$
C_Q	=	non-dimensional torque coefficient, $C_Q = \frac{Q}{\rho\pi R^3(\Omega R)^2}$
C_{CPU}	=	simulation time cost per cpu [s]
f_0	=	enstrophy filter cutoff frequency [Hz]
J	=	advance ratio, $J = \frac{V_\infty}{\Omega R}$
n	=	revolutions per minute [rpm]
N_{cr}	=	critical boundary layer disturbances integral amplification
N_s	=	number of particle sources shed from the lifting lines per time-step

*Ph.D. Candidate, Department of Mechanical and Aerospace Engineering, AIAA Member
†Assistant Professor, Department of Mechanical and Aerospace Engineering
‡Aerodynamics Research Engineer, Aerodynamics, Aeroelasticity and Acoustic Department
§Associate Professor, Department of Mechanical and Aerospace Engineering, AIAA Member.

Q = torque [Nm]
r = reference coordinate along the propeller radius [m]
R = propeller radius, $R = 7.5$ cm
Re_c = rotational chord-based Reynolds number, $Re_c = \frac{c\Omega r}{\nu}$
s_{C_T} = non-dimensional sectional thrust along the bladespan
T = thrust [N]
V_z = velocity field component in the z axis [m/s]
V_∞ = axial inflow velocity [m/s]
x = reference axis in the propeller's wake radial direction [m]
z = reference axis in the propeller's wake axial direction [m]
β = blade twist angle [°]
Γ = blade dihedral angle [°]
Δt = time-step [s]
δ = relative deviation [%]
Λ = blade sweep angle [°]
ν = air kinematic viscosity [m^2/s]
ρ = air density [kg/m^3]
$\Delta\psi$ = azimuthal angle swept by the blades per time-step [°]
Ω = propeller angular speed [rad/s]
$\overline{(\cdot)}$ = time-averaged quantity

II. Introduction

Small unmanned air vehicles (UAVs) are becoming increasingly popular in various applications, including urban air mobility (e.g. [1]), territorial monitoring (e.g. [2]), agriculture (e.g. [3]), and even military operations (e.g. [4]). This growing popularity is accompanied by a substantial increase in the market size, expecting to reach a value of 120B$ by 2032 [5]. Although it is still an emerging research field, numerous studies exist on the performance of small drones (e.g. [6–12]), which is far from straightforward, especially from the aerodynamic perspective. The propulsion system of these drones typically consists of multiple fixed-pitch propellers characterized by small dimensions. Due to this latter feature, the propellers often exhibit low chord-based Reynolds numbers (Re_c) along the entire blade span direction. For Re_c below 500,000, complex transitional phenomena occur on their blades' surfaces [13, 14], affecting the overall performance of the drone. In particular, if Re_c is between 50,000 and 500,000, it has been observed that the laminar boundary layer detaches close to the leading edge, then transition to turbulent and reattaches further downstream, forming a region known as a laminar separation bubble. If the Reynolds number is further reduced below 50,000, it is possible that the energy in the freestream is insufficient to cause flow transition, and thus after the flow may not reattach, generating a wide wake region of separated flow characterized by strong and periodic vortical structures.

In the present work, an isolated small drone propeller, characterized by Re_c ranging from 5,000 to 25,000 along the bladespan, is investigated in hovering and axial inflow with multiple techniques. In a first instance, an experimental campaign was carried out in Politecnico di Torino to obtain the performance data with dedicated load sensors and the induced velocity field with the use of planar Particle Image Velocimetry (PIV). Subsequently, mid-high fidelity CFD simulations were conducted with the URANS modeling, aiming to match the experimental results. The URANS simulations were computed through an overset mesh approach, taking into account the SST $k-\omega$ turbulence model [15] coupled with the $\gamma - Re_\theta$ transitional model [16]. The two methods were then compared with a the low-fidelity vortex particle code denominated VULCAINS v0.5 [17–19], in-house-built by ONERA.

The vortex particle methods (VPM) are meshless methods which solve the vorticity form of Navier-Stokes equations in a lagrangian scheme. This methodology is particularly suitable for vorticity-governed flows, accurately preserving vortical structures and being free of the numerical dissipation associated to conventional mesh-based approaches like Reynolds-Averaged Navier-Stokes (RANS) simulations and Large-Eddy Simulations (LES). This method has been shown to achieve a good accuracy both in low fidelity conceptual design (e.g. [20–22]) and in high fidelity applications (e.g. [23–25]) while offering a considerable speed up over classic higher fidelity approaches. VULCAINS features different novelties with respect to the already available VPM solvers. Among them, the code implements the Diffusion Velocity Method (DVM) as an alternative diffusion scheme to account for the viscous effects in the flow. This scheme aims to replace the state-of-art schemes as the Particle Strength Exchange (PSE), enhancing the VPM precision in capturing the diffusion effects, especially at the external boundaries of the computational domain. Furthermore, the

DVM does not require a frequent redistribution of the particles, which conveniently prevents from the exponential growth of the number of particles in the domain. The code additionally provides for an enstrophy control filter for the particle control which results to be particularly efficient in regions of the flow that are highly turbulent, such as the wake of hovering propellers. Further parameters can be adjusted by the user in order to speed up the computations or improve their accuracy. To do so, it is necessary to investigate the isolated influence of the most relevant parameters. A baseline case is hence defined for a first comparison with the experiments and URANS simulations. After this first comparison, the influence of each parameter on the solution is thoroughly investigated, focusing on the performance, the induced flow field and the computational cost. Among the numerous input parameters, the choice of aerodynamic polars for the lifting lines simulating the blades is surely a critical passage. In this work, the choice fell on using the free software XFoil [26], due to its high computational speed, ease of use, and reliability at low Reynolds numbers, already proven in previous studies [27, 28]. The predictions using XFoil usually match the higher fidelity computations, at least up to angles of attack close to the stall angle [29]. The set of airfoil polars are expected to produce accurate results if the angle-of-attack of the propeller blades is low-to-moderate, such as in classical axial flow conditions. On the contrary, for high angle-of-attack conditions, the airfoil polars data are not expected to capture the complex 3D phenomena involved at the blade sections near the stall conditions [30], which may happen in hovering or non-axial flow conditions. With the use of the set of polars computed with XFoil, the influence of other parameters in VPM simulations was analyzed, particularly including: the number of vorticity sources generated per each time-step (N_S), the azimuthal angle swept per each time-step ($\Delta\psi$), the order of integration in time, the velocity diffusion scheme, the turbulent viscosity model for the small-scales modeling and finally the intensity of the enstrophy control filter (f_0). The influence of the listed parameters is documented with the calculation of the relative deviation with respect to the baseline case. In addition, aerodynamic loads time histories, sectional loads along the bladespan, and velocity profiles will be used to highlight the most relevant deviations.

The remainder of the paper is organized as follows: in section II, an introduction to Vortex Particle Methods is presented. The experimental setup, the numerical framework for the URANS simulations and the VPM simulations are described in section III. Section IV presents the results of the comparison of the three methodologies and the influence of the different input parameters on the VPM results. Finally, in section IV, the conclusions and some future outlooks are drawn.

III. Theoretical background

A. Vortex Particle Method

In this section, the theory behind the viscous vortex particle methods is summarized, with a focus on the peculiar features which characterize the VULCAINS code.

1. Governing Equations

A viscous, unbounded and incompressible flow dominated by vorticity can be resolved by formulating the Navier-Stokes equations into their vorticity form. This is done by taking the curl over the original momentum equation from a lagrangian point of view, leading to the expression in eq.1 that is not dependent on the pressure field, given $\vec{\omega} = \vec{\nabla} \times \vec{U}$ is the flow vorticity.

$$\frac{D\vec{\omega}}{Dt} = \frac{\partial \vec{\omega}}{\partial t} + \left(\vec{U} \cdot \vec{\nabla}\right)\vec{\omega} = \left(\vec{\omega} \cdot \vec{\nabla}\right)\vec{U} + \nu\Delta\vec{\omega} \tag{1}$$

The material derivatives expressed in eq.1, are well suited for a lagrangian description. The two terms on the right-hand-side respectively account for the vortices stretching and the viscous effects in the flow. The flow is spatially discretized by introducing a finite set of particles, each one acting as a radial-basis gaussian function of core radius σ. Each particle induces velocity at any point of the flowfield through the Biot-Savart law. This discretization process is equivalent to a spatial filter of size σ. Hence, all flow structures smaller than σ cannot be solved and they represent the unresolved scales. For the VPM to converge, it is necessary that the particles overlap [31], $i.e.$ the inter-particles distance h must satisfy $h < \sigma$.

Eq. 1 can be hence filtered and a term $\vec{E}_{trunc}$ appears on the right-hand-side. This term, explicited in eq. 2, represents the error between the resolved and unresolved quantities due to the filtering of the small scales. A turbulent viscosity model can be used for its approximation since it represents the enstrophy loss transferred to the small scales.

$$\vec{E}_{trunc} = -\vec{\nabla} \cdot \left(\nu_t \left[\left(\vec{\nabla} \times \tilde{\vec{\omega}} \right) + {}^{t} \left(\vec{\nabla} \times \tilde{\vec{\omega}} \right) \right] \right) \tag{2}$$

In eq. 2 the $\tilde{\vec{\omega}}$ represents the filtered vorticity, while ν_t the turbulent kinematic viscosity. The second term on the right-hand-side is here neglected [32].

Each particle is characterized by a strength $\vec{\alpha}$, obtained by integrating the vorticity of the flow in the volume of the particles. The vorticity of the flow can be in turn retrieved from the particles strength, taking into account a gaussian distribution for the spatial filter. The evolution equation of the particles' strength is reported in eq.3.

$$\frac{d\vec{\alpha}_i}{dt} = \left(\vec{\alpha}_i \cdot {}^{t}\vec{\nabla} \right) \vec{U}_i + V_i \vec{\nabla} \cdot \left(\left(\nu + \nu_{t_i} \right) \left(\vec{\nabla} \times \vec{\omega}_i \right) \right) \tag{3}$$

The flow velocity is obtained with the Helmotz Decomposition Theorem as $\vec{U} = \vec{U}_\infty + \vec{u}_\phi + \vec{u}_\psi$, where the last two terms corresponds respectively to the curl-free and solenoidal parts of the total velocity. No irrotational sources are considered in this approximation, the only contribution to the total velocity is hence the divergence-free velocity which is induced by the particles and is obtained from the Biot-Savart law: $\vec{u}_\psi = \int_V \frac{1}{4\pi r^3} \vec{\omega} \times \vec{r}\, dV$ and the freestream velocity. The solenoidal velocity is regularized by a smoothing function, obtained directly from the spatial filter.

The particles are advected in the flow accordingly to the total velocity. In this work, the curl-free velocity sources $\vec{u}_\phi$ are neglected, thus leading to eq.4 to calculate the position of each particle $\vec{x}_i$.

$$\frac{d\vec{x}_i}{dt} = \tilde{\vec{U}}(\vec{x}_i, t) \approx \vec{U}_i = \vec{U}_\infty + \vec{u}_{\psi_i} \tag{4}$$

The direct solution of the terms involved in the vorticity equation is costly, being the inter-particles interaction of the order of $O(N^2)$. The Fast Multipole Method (FMM) can be used to efficiently reduce these interactions and reduce the cost to approximately $O(N)$. The open source module ExaFMM [33] was considered for the purpose, parallelized with OpenMP.

2. Viscous Treatment of the Flow

One of the principal advantages of the VPM, in comparison to other potential methods, lies in its intrinsic ability to account for viscous effects. The diffusion term of the VPM equations can be solved to simulate viscous interactions between vortex structures. The VULCAINS code implement 3 different schemes for the diffusion modeling: the Core Spreading Method (CSM), the PSE and DVM.

The CSM method was originally developed by Leonard [34] to include the viscous effects in the 2D cases. The viscous effects encountered in the flow are modeled as a growth of the particles which move away from the vorticity source, resulting in a coarser solution of the flow in the far field. Such enlarged particles contribute to a smoother induction, leading to a more stable simulation. However, if on one side the method is of easy implementation and theoretically it reduces the computational cost, non-negligible errors are usually present in the FMM approximations. To maintain FMM accuracy, it is necessary to take into account the effect of larger particles over greater distances, thus increasing the number of particle-to-particle interactions and, consequently, the computational cost.

The PSE, developed by Mas-Gallic [35], is one of the most common methods to model the viscous effects in the VPM. The vorticity is exchanged among adjacent particles to diffuse it in the flow. The precision of the method mainly depends upon the spatial filter and the mandatory redistribution of the particles, which also represents the major drawback of this method. The method in fact poorly behaves at the boundaries of particles' clusters, denying the possibility of diffusing the vorticity beyond the boundaries of such clusters. Frequent redistribution of particles are indeed required to expand the domain filled by the particles, significantly increasing the computational cost.

The DVM aims to accurately compute the diffusion effects in the flow, without requiring a frequent redistribution or excessive growth of the particle size. Its main features are here summarized. For a detailed description, see the work [19].

The DVM rewrites the vorticity equation as an advection equation by incorporating part of the diffusion term inside the material derivatives. The unfiltered vorticity equation (eq.1) can be re-written considering a diffusion velocity $\vec{u}_d$ as done in eq.5.

$$\frac{\partial \vec{\omega}}{\partial t} + \vec{\nabla} \cdot \left(\left(\vec{U} + \vec{u}_d \right) \times \vec{\omega} \right) = \left(\vec{\omega} \cdot \vec{\nabla} \right) \vec{U} + \vec{\nabla} \cdot \left(\left(\nu \vec{\nabla} + \vec{u}_d \right) \times \vec{\omega} \right) \tag{5}$$

The diffusion velocity aims to represent the diffusion occurring in the rotation plane of the particles and can be written as $\vec{u}_d = -\nu \frac{\vec{\nabla}||\vec{\omega}||}{||\vec{\omega}||}$. In this fashion $\vec{u}_d$ becomes singular when the vorticity becomes null, which usually happens at the edge of the domain [36, 37]. This is avoided following [38] by imposing: $\frac{1}{||\vec{\omega}||} \approx \frac{||\vec{\omega}||}{\omega_0{}^2+||\vec{\omega}||^2}$, ω_0 being a cutoff vorticity set to a small fraction of the highest vorticity value in the flow. The diffusion velocity hence does not result to be divergence free as the induced velocities. Differently to what is done in previous works (e.g. [36, 37]), in VULCAINS the diffusion velocity is directly computed instead of updating the particles volume solving the strength α for each particle. In this fashion, the volume of the particles V has to evolve according to $\frac{dV}{dt} = \int_V \vec{\nabla} \cdot \vec{u}_d \, dV$.

The diffusion velocity calculated in a discrete formulation for the particles is so added to the total velocity. The complete system of equations which governs the particles' evolution with the DVM is reported in the system of eqs. 6.

$$\begin{cases} \frac{d\vec{\alpha}_i}{dt} = \left(\vec{\alpha}_i \cdot {}^t\vec{\nabla}\right)\vec{U}_i + V_i\vec{\nabla} \cdot \left(\left(\nu\vec{\nabla} + \vec{u}_d\right) \times \vec{\omega}\right) \\ \frac{d\vec{x}_i}{dt} = \vec{U}_\infty + \vec{u}_{\psi_i} + \vec{u}_{d_i} \\ \frac{dV_i}{dt} = V_i\vec{\nabla} \cdot \vec{u}_{d_i} \end{cases} \tag{6}$$

3. Turbulent Viscosity Modeling

The turbulent viscosity used to account for the truncature error and closure of the VPM equations is computed through a model, in order not to solve the smallest scales as in a DNS [39]. The mixing length theory [40] states that the turbulent viscosity ν_t can be calculated as: $\nu_t \propto \Delta^2||\bar{\bar{S}}||$, with $\Delta \approx \sigma$ the flow filter width and $||\bar{\bar{S}}||$ the strain tensor. Depending of the resolved scales, ν_t can be approximated with the use of the Smargorinsky constant C_s: $\nu_t = C_s\sigma^2||\bar{\bar{S}}||$. Many LES turbulent viscosity models are available in literature, but the limited flow quantities resolved in the VPM restricts the number of possibilities. Three models were implemented in VULCAINS: the Smargorinsky model [41], the Mansour model [42] and the Vreman model [43]. These three models come from the hypothesis on homogeneus and isotropic turbulence and all depend on the constant C_s, resulting in the issue of emphasizing or downplaying the role of turbulence in the flow. In the present work, the influence of the three models on the final results is analyzed for the small propeller study case, along with the influence of the previously mentioned parameters.

4. Particles Control

In order to preserve the divergence-free nature of the modeled flows and prevent numerical instabilities, it is necessary to intervene with a redistribution, resizing or re-orientation of the particle with respect to the vorticity field. In this section, an enstrophy control filter developed in VULCAINS is introduced. The intensity of this filter can be increased or decreased by the user through a single constant parameter f_0. This filter results to be of significant impact on the flow solution mostly in highly turbulent flows, as the wake of a hovering propeller or at high Reynolds numbers. In his work [44], Pedrizzetti proposed an approach for a filter only based on the re-orientation of particles, with a minor side effect on their magnitude. In the VULCAINS code, a new approach based on the active control of the enstrophy ($\mathcal{E}$) is instead proposed. After each sub-iteration of the Runge-Kutta integration scheme, the particles strength is adjusted both in magnitude ($||\vec{\alpha}||$) and direction ($\hat{\alpha}$), according to: $\vec{\alpha}_{new} = \vec{\mathcal{F}}_{\mathcal{E}}(\vec{\alpha}, \Delta t_0) = \mathcal{F}_{mag}(\vec{\alpha}, \Delta t_0)\vec{\mathcal{F}}_{dir}(\vec{\alpha}, \Delta t_0)$. The magnitude $\mathcal{F}_{mag}$ and direction $\vec{\mathcal{F}}_{dir}$ filters are defined as functions of the particle strength and depend also upon the time interval Δt_0 over which they are applied. The filters can be initially defined as in eq. 7, being f_{mag} f_{dir} the cutoff frequencies of the two filters.

$$\begin{cases} \mathcal{F}_{mag}(\vec{\alpha}, \Delta t_0) = ||\vec{\alpha}|| \left(1 - \Delta t_0 f_{mag}\left(1 - \frac{||\vec{\alpha}_{div-free}||}{||\vec{\alpha}||}\right)\right) \\ \vec{\mathcal{F}}_{dir}(\vec{\alpha}, \Delta t_0) = (1 - \Delta t_0 f_{dir})\hat{\alpha} + \Delta t_0 f_{dir}\hat{\alpha}_{div-free} \end{cases} \tag{7}$$

It is now due to determine the particle strength $\vec{\alpha}_{div-free}$ which permits to induce a divergence-free flow. The direction $\hat{\alpha}_{div-free}$ can be chosen accordingly to the direction of the divergence-free vorticity field $\vec{\nabla} \times \tilde{\vec{U}}$. The magnitude $||\vec{\alpha}_{div-free}||$ can be instead related to the enstrophy of the flow ($\mathcal{E} = \int_{R^3} ||\vec{\nabla} \times \vec{U}||^2 dV$) and the enstrophy of the particles ($\mathcal{E}_f = \int_{R^3} ||\vec{\omega}||^2 dV$) in their filtered and self-induced forms ($\tilde{\mathcal{E}}_0$, $\tilde{\mathcal{E}}_{f_0}$) as follows: $\frac{||\vec{\alpha}_{div-free}||}{||\vec{\alpha}||} \approx \sqrt{\frac{\tilde{\mathcal{E}}_0}{\tilde{\mathcal{E}}_{f_0}}}$. The enstrophy control filter $\vec{\mathcal{F}}_{\mathcal{E}}$ can be expressed as a function of the introduced quantities as in eq. 8.

$$\vec{\mathcal{F}}_{\mathcal{E}}(\vec{\alpha}, \tilde{\vec{U}}, \Delta t_0) = \left(1 + \Delta t_0 f_{mag}\left(\sqrt{\frac{\tilde{\mathcal{E}}_0}{\tilde{\mathcal{E}}_{f_0}}} - 1\right)\right)\left((1 - \Delta t_0 f_{dir})\vec{\alpha} + \Delta t_0 f_{dir}\frac{||\vec{\alpha}||}{||\vec{\nabla} \times \tilde{\vec{U}}||}\vec{\nabla} \times \tilde{\vec{U}}\right) \tag{8}$$

If the two enstrophies match or the magnitude filter equals to 1, only the direction filter is applied. On the other hand, if the particle is aligned with the local divergence-free vorticity field of f_{dir} is null, only the magnitude filter is applied.

Using constant values of f_{mag} and f_{dir} might lead to inadequate adjustements of the particles properties trying to match the local divergence-free fields. If the particles are not already close to the vorticity field, excessively sudden and often insufficient changes might occur to their magnitude and direction. The cutoff frequencies are hence written as a function of the particles' own enstrophy, calibrating their properties changes with respect to this quantity. The magnitude cutoff frequency is tailored according to the particles strength, to avoid the filtering of weak particles and overlooking of the strong ones: $f_{mag_i} \propto \mathcal{E}_{f_i} - \overline{\mathcal{E}}$ for each i particle, being $\overline{\mathcal{E}}$ the mean enstrophy of the flow. The direction cutoff frequency is instead updated based on the angle between each particle orientation and the vorticity field. The non-constant cutoff frequencies can be hence written as in the system of eqs. 9, given f_{mag_0} and f_{dir_0} user-defined constants, $\mathcal{E}_0$ the maximum enstrophy among the particles immediately shed by the propeller blades.

$$\begin{cases} \Delta t_0 f_{mag_i} = f_{mag_0}\frac{\tilde{\mathcal{E}}_i - \overline{\mathcal{E}}}{\mathcal{E}_0 - \overline{\mathcal{E}}} \\ \Delta t_0 f_{dir_i} = \frac{f_{dir_0}}{\pi} arccos\left(\frac{\tilde{\mathcal{E}}_i}{||\vec{\alpha}_i||||\tilde{\vec{\nabla}} \times \tilde{\vec{u}}_i||}\right) \end{cases} \tag{9}$$

As a best practice, the authors suggest the use of $f_{mag_0} = \Delta\psi f_0$ and $f_{dir_0} = 2\Delta\psi f_0$ for the rotating lifting lines, being $\Delta\psi$ the azimuthal angle swept per each time-step. The enstrophy filter is consequently controlled by the user varying the cutoff frequency f_0, which must be increased for highly turbulent flows as the propeller's wake in hovering condition.

5. Coupling with Lifting Lines

The propeller blades are simulated with a lifting line module, added to VULCAINS for its low computational cost and simplicity. The two blades are represented with a different lifting line which is defined from $r/R = 0.2$ to $r/R = 1$ and is split into small segments with an hyperbolic tangent function from the root to the tip, where the smallest segments are located. The lifting lines are moved according to their own solid and rotation to simulate the propeller motion. As the blades rotate around the rotation center, discrete particle sources are shed from the lifting lines with a vorticity value that preserve the local circulation calculated on the corresponding lifting line element. The local angle of attack is computed by taking into account the kinematic velocity of the lifting lines, the freestream velocity and the induced velocity from the particle sources. The aerodynamic loads are computed on each segment thanks to a 2D polar database, which links the angle of attack and the local Reynolds and Mach number to a value of lift and drag. Once the loads are computed, it is possible to calculate the associated circulation with the Kutta-Joukowski theorem. According to Kelvin's theorem, the introduction of a solid in the flow needs to be balanced with vorticity generation due to the variations of circulation in the lifting lines. To respect this, particle sources are shed from the lifting lines and set free in the wake. The particles are generated with a distribution which can be also independent from the lifting lines discretization. In the current application, it is appropriate to shed more particles close to the blade tip, in order to properly capture the tip vortex dynamics. The particles generated in the wake induce in turn a velocity on the blades elements, affecting the angle of attack and consequently the loads and circulation.

IV. Methodology

A. Experimental Campaign Setup

The experiments were performed in the "Ferrari" open circuit wind tunnel at Politecnico di Torino. The setup is the same described in [6, 45].

The propeller holding support was mounted in the center of the test section at a distance of 44 cm from the test chamber inlet. A preliminary characterization of the flow has revealed that the mean flow profile is uniform across a span of about 30 cm at this distance, with a turbulence intensity level below 1% at inflow velocities between 1 and 8 m/s.

Focusing on the propeller and its support, the main components are presented in figure 1 and herein briefly described. The propeller was 3D printed in VisiJet Armor M2G-CL resin. The model's geometry was defined by taking the propeller employed in [46] as a reference and then scaling it for the current purpose to a propeller with a radius $R = 7.5$

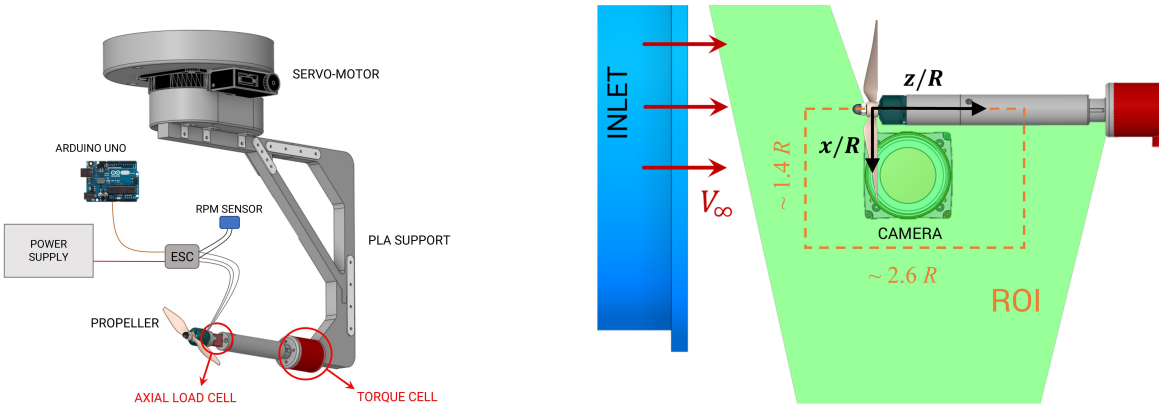

Fig. 1 Schematic representation of the propeller support.

cm. It derives from a two-bladed APC-96 model, by reshaping each profile from $r/R = 0.2$ to the tip with a NACA 4412 profile, being r the radial reference coordinate along R. An elliptical root section is merged with such profiles starting from the hub to the station $r/R = 0.2$. The blades' main geometric features are reported in figure 2 in terms of non-dimensional chord c/R, twist angle , sweep angle Λ and dihedral angle Γ distributions along the bladespan direction.

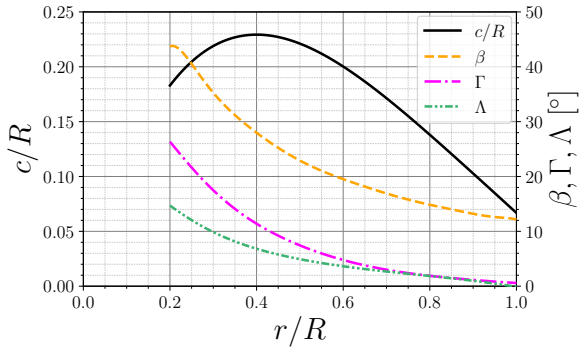

Fig. 2 Blades main geometric features along the bladespan direction.

Two load sensors were used to evaluate the propeller's loads: a bi-directional axial load cell Futek LSB201 was chosen for the thrust measurements and a Futek TFF400 torque sensor for the torque measurements. The rotational speed Ω of the motor was measured using an Hobbywing RPM sensor. The propeller's thrust and torque are acquired over a sampling time of 120 seconds at a sampling frequency of 10 kHz.

The flow field surrounding the propeller was investigated through planar PIV in a region of interest (ROI) which extended for approximately $2.6R$ in the stream-wise direction and $1.4R$ in the cross-wise direction, as illustrated in the right side of figure 1. The acquisition frequency was set to 15 Hz. The origin of the reference system used for the PIV fields is placed in correspondence of the propeller's hub and the two coordinates x and z are normalized with respect to the propeller's radius R. The inflow velocity (V_∞) direction aligns with the z axis. The tests were conducted at a fixed n = 5014 rpm, while V_∞ was imposed equal to 0 m/s or 3.4 m/s, to respectively simulate the hovering condition ($J = 0$) and the axial inflow condition at a value of $J = 0.1$.

B. URANS Simulations Setup

The URANS simulations of the rotating propeller were performed using the elsA solver developed by ONERA [47]. The computational workflow including grid generation, simulation and postprocess was executed using toolchain

MOLA v1.18*. Among the available turbulence models, the SST $k-\omega$ was chosen as one the most widely used for the external aerodynamics and since it has proven to be reliable in propellers simulations [48, 49]. In particular, it was coupled with the $\gamma - Re_\theta$ transition model to attempt to capture the laminar to turbulent transition which characterizes the flow around propellers' blades at these low Reynolds numbers.

An overset meshing or "Chimera" technique was used to simulate the blades motion. The two blades were simulated from $r/R = 0.2$ to their tip and the spinner was not hereby considered, in order to reproduce the same geometry evaluated also in the VPM simulations.

The two rotating meshes were generated with a structured grid starting from a wall cell height that guarantees a Δy^+ of around 0.2 in the considered operative conditions. The grid was extruded for a normal-to-wall distance of 0.12 R.

The rotating meshes were consequently overlapped on a static cartesian background mesh. This mesh extended for $20R$ from the rotating center of the propeller. A further refined cylindrical region was then generated to adequately capture the flow evolution in the wake. The cells in this region have characteristic dimensions which are very similar to the outermost cells of the rotating domain, in order to ensure an exchange of information between the two meshes which minimizes numerical dissipation. This refinement region significantly contributed to the total amount of grid points, increasing the simulations computational cost. A slice of the final mesh close to propeller is reported in figure 3.

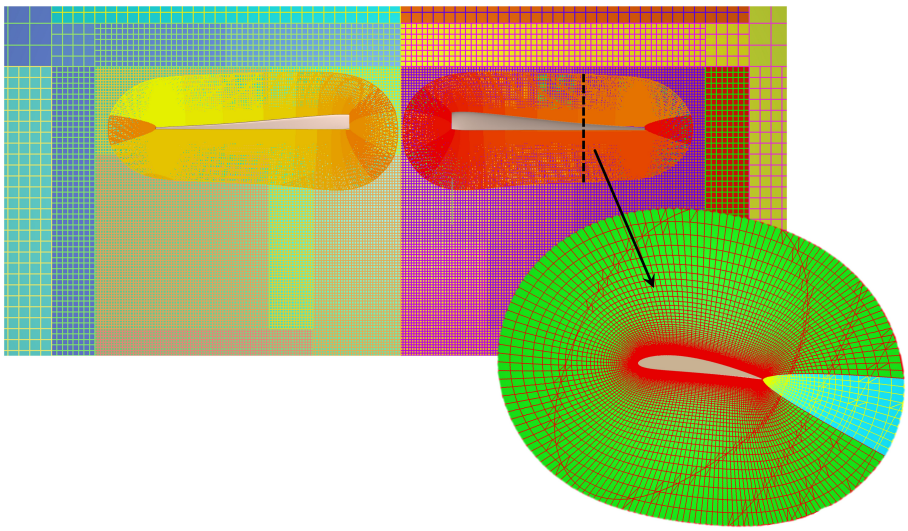

Fig. 3 Computational grid around the propeller.

1. Spatial and temporal discretization

A spatial and temporal discretization study was carried out on both advance ratios, taking into account three different meshes and three associated time-steps. The tests were conducted for 30 revolutions and the loads were averaged over the last 10 revolutions. The meshes differ mainly for the number of points on the blades surfaces and in the extrusion direction. Consequently, the refined background is adapted according to the mesh features in the rotating domain. The time-step value in seconds is calculated as $\Delta t = \Delta\psi/(6n)$, being $\Delta\psi$ the azimuthal angle swept by the blades per time-step. The discretization parameters and the resulting time-averaged thrust and torque coefficients are reported in table 1.

The time-averaged non dimensional loads $\overline{C_T}$ and $\overline{C_Q}$ present almost negligible differences between M2 and M3 both in hovering (J=0) and axial inflow (J=0.1). The loads evaluated for the M1 case instead results to slightly deviate from the other two cases, with relative errors up 5-6% for $\overline{C_T}$ and 7-8% for $\overline{C_Q}$ in hovering condition. The M2 mesh was consequently chosen for the comparison with the experimental results and the baseline VPM case, presenting almost equivalent integral loads values of the most refined mesh M3 but with a considerable decrease in computational cost.

*https://github.com/onera/mola

Table 1 Grid and Time-Step Convergence Parameters.

			J=0.0		J=0.1	
Mesh Name	Number of Cells	$\Delta\psi$ [°]	$\overline{C_T}$	$\overline{C_Q}$	$\overline{C_T}$	$\overline{C_Q}$
M1	8.3 Millions	1.5	1.45e-02	2.21e-03	1.03e-03	2.20e-03
M2	17.1 Millions	0.75	1.36e-02	2.39e-03	9.97e-03	2.11e-03
M3	31.8 Millions	0.25	1.35e-02	2.38e-03	9.97e-02	2.11e-03

C. VPM Simulations Setup

The VPM simulations were conducted with the VULCAINS code in-house-built by ONERA [17, 18]. The propeller's blades are simulated with two rotating lifting lines positioned at the first fourth of their chord distribution. The number of blades, the propeller radius, the airfoils distribution along the radius and the chord and twist angle distributions are needed to define the lifting lines. A further fundamental parameter is the 2D polars database, which in the present case is retrieved with the use of XFoil. The polars are calculated for the Reynolds numbers of 10,000, 20,000 and 30,000 and angles of attack from -5° to 20° with a 0.1° angle step. The curves are obtained by considering the boundary layer disturbances integral amplification evaluated at the transition location (N_{cr}) equal to 5. The loads solution to a given angle of attack is the result of the interpolation among these curves. If the local angle of attack or Reynolds number falls out of the polars range, the solution is extrapolated between the chosen polars and a dataset of polars obtained for the NACA0012 airfoil in post-stall condition [50]. Once the lifting lines and the operative conditions are defined, it is necessary to setup the parameters related to the VPM computation. The most relevant include the number of particle sources shed by each blade at each timestep (N_s), the azimuthal angle swept per timestep ($\Delta\psi$), the order of the Runge-Kutta scheme for the integration in time, the diffusion modeling scheme, the turbulent viscosity model and finally the cutoff frequency (f_0) to regulate the intensity of the enstrophy control filter. One of the advantages of VPM is that these parameters do not need a calibration for each different test case and the same values might be used in various applications. However, their choice might affect the computations in terms of final results or computational cost. In the present work, the first scope is to perform VPM simulations using some baseline input parameters in the attempt of matching the experimental and the URANS predictions of the propeller performance and induced flow field. In a second instance, the aim is to analyze how the variation of these parameters may affect the final solution and the computational cost with respect to the baseline case.

1. Definition of a baseline case

In this section, the baseline case is introduced. The two lifting lines corresponding to the two propeller's blades are discretized with N=100 elements, where the root and the tip segments present a length of $2(0.8R)/(N - 1)$, while the length of the intermediate segments was defined with a hyperbolic tangent function between the extremes. In the considered region of the blade, between $r/R = 0.2$ and $r/R = 1$, the blade is made of NACA 4412 airfoils. The lifting lines are rotated by $\Delta\psi$ around the rotation center per each time-step, shedding in the wake N_s particle sources. The time-step Δt is calculated from $\Delta\psi$ as done for the URANS computations: $\Delta t = \Delta\psi/(6n)$. The values chosen for the baseline input parameters in the VPM computations are reported in table 2.

Table 2 Input parameters for VPM baseline case

2D polars	N_S	$\Delta\psi$ [°]	Integration Order	Diffusion Scheme	Turbulent Viscosity Model	f_0
XFoil (N_{cr}= 5)	40	5	3	DVM	Vreman	0.75

The VPM simulations were conducted for the baseline case at the same operative conditions evaluated in the experimental campaign and the URANS computations.

2. Evaluation of the input parameters influence

The input parameters listed in table 2 are varied one at a time to investigate their isolated influence with respect to the baseline case. The number of sources per time-step N_S was initially varied between 20 and 60, while $\Delta\psi$ was varied between 2.5° and 10°. The time integration order of the Runge-Kutta scheme was instead compared between the 1^{st} and the 4^{th}. The influence of the diffusion scheme and the turbulent viscosity model influence was analyzed by comparing the implemented models in VULCAINS. Particularly for the choice of the diffusion scheme, the DVM model was compared with CSM and PSE. For what regards the turbulent viscosity model, the Vreman model was compared with the Mansour and the Smargorinsky models. Finally, the enstrophy filter cutoff frequency f_0 was varied from 0.25 to 1.25. The impact on the final solution was evaluated in terms of propeller loads, induced velocity in the wake and computational cost. The loads are compared with respect to the baseline case in terms of time-averaged non-dimensional thrust and torque coefficients ($\overline{C_T}$, $\overline{C_Q}$), non-dimensional thrust standard deviation (σ_{C_T}) and sectional time-averaged non-dimensional thrust distribution along the bladespan direction ($\overline{s_{C_T}}$). The induced velocity in the wake is evaluated as a time-averaged non-dimensional axial velocity profile ($\overline{V_z}/\Omega R$) extracted at z/R = 1. Finally the computational cost is evaluated in terms of total time required per core (C_{CPU}) to complete the simulation. The averaging operation of the listed quantities was carried out over the last 30 revolutions at both advance ratios. The comparison is finally carried out by computing the relative deviation of the listed quantities $\delta(\cdot)$ with respect to the baseline values. In the case of scalar quantities such as $\overline{C_T}$, $\overline{C_Q}$, $\overline{s_{C_T}}$ and C_{CPU}, the relative deviation is computed as a relative error with respect to the baseline case. On the other hand, in the case of the sectional thrust distribution $\overline{s_{C_T}}$ and the axial velocity profile $\overline{V_z}/\Omega R$, the relative deviation is computed as a mean relative deviation, thus evaluating point-by-point the relative error in absolute value with respect to the baseline case.

V. Results

The first subsection reports the comparison between the experimental results, the URANS simulations results, and those related to VPM simulations using the baseline input parameters listed in table 2. The comparison is made in terms of time-averaged non-dimensional loads and axial velocity field along the z axis. Given the cylindrical symmetry of the time-averaged flow field in the analyzed operative conditions, a 2D slice of the URANS and VPM fields corresponding to the region experimentally analyzed with planar PIV is exclusively displayed for the comparison. The following subsection focuses instead on the influence of the input parameters on the VPM solution. This study is carried out with the aid of two tables containing the relative deviations of $\overline{C_T}$, $\overline{C_Q}$, $\overline{s_{C_T}}$, ($\overline{V_z}/\Omega R$) and C_{CPU} with respect to the baseline case. The influence of each parameter is then analyzed in details with the eventual aid of dedicated figures if the relative deviations resulted to be of significant magnitude.

A. Comparison among PIV, URANS and VPM

The colormaps of the axial velocity fields in hovering (J=0) and axial inflow (J=0.1) and the velocity profiles extracted at z/R = -0.5, 0.7 and 1.5 are displayed in figure 4. In the same figure, the time-averaged non-dimensional thrust $\overline{C_T}$ and torque values $\overline{C_Q}$ are reported for the different approaches.

In particular, the URANS simulations tend to overestimate both the thrust and torque in hovering and axial inflow. In hovering, the deviation is more pronounced, being around +5.5% for $\overline{C_T}$ and +8.3% for $\overline{C_Q}$. Such relative error decreases in the case of axial inflow, dropping to +3.2% for $\overline{C_T}$ and +3.9% for $\overline{C_Q}$. Similar considerations can be made by analyzing the axial velocity field or the related velocity profiles for a quantitative comparison. The greatest differences are again found in the case of J = 0 especially in the core of the wake, between $x/R > 0.3$ and $x/R < 0.6$. As it can be observed in the velocity profiles extracted at z/R = 0.7, the relative error between the experimental velocity and the URANS simulations is of the order of 8%. For $x/R > 0.6$, the two velocity profiles instead tend to overlap, thus indicating a good match of the wake width prediction in the radial direction between the two methodologies. At z/R = 1.5, the URANS overestimates the axial velocity in the wake with errors around +14%. At this distance, the velocity profiles at $x/R > 0.6$ do not smoothly overlap as previously observed, but instead show a slight difference indicating that the experimentally measured wake is on average wider in the radial direction compared to the URANS wake. The absence of the spinner in the URANS simulations might have played a role in this context. The wake is in fact free to expand towards x/R = 0, resulting in a time-averaged topology that is certainly different if compared to a case where the spinner is also simulated. This difference in the simulation setup might also affect the maximum velocity in the wake, which is experimentally reached around z/R = 0.8-0.9, while, in the URANS simulations, the velocity increases at least up to z/R = 1.7-1.8.

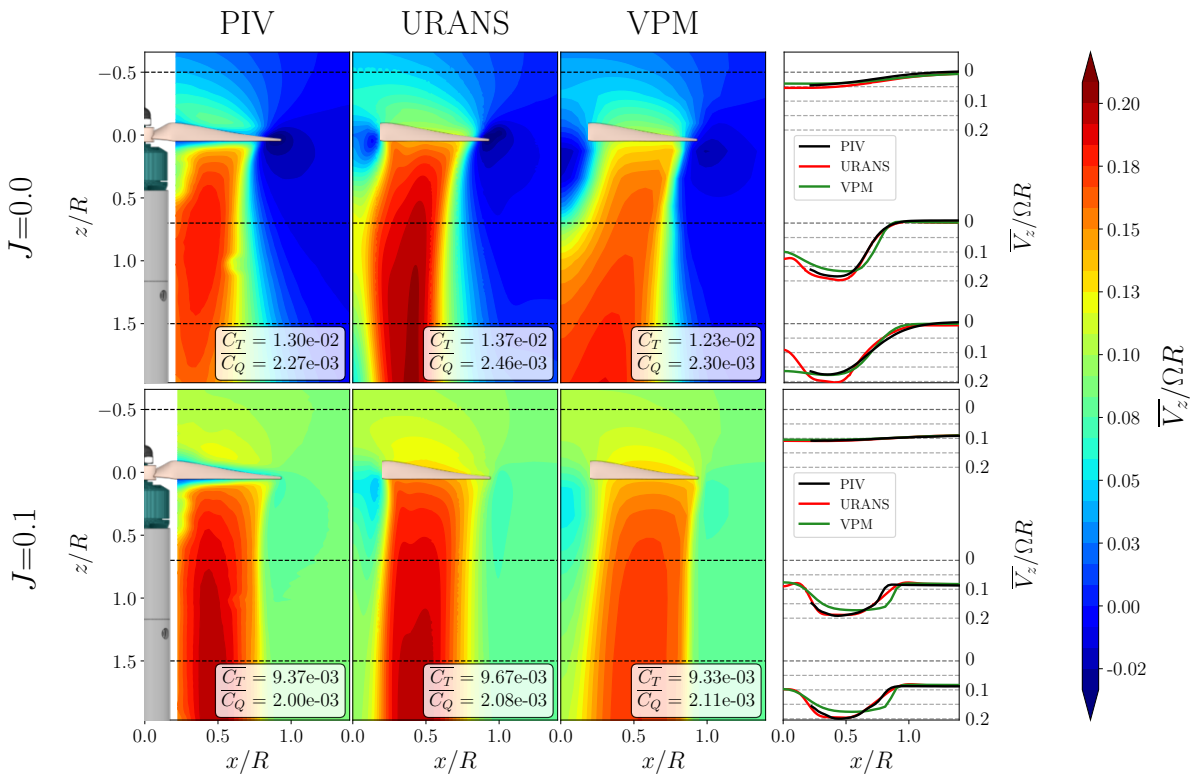

Fig. 4 Colormaps of the normalized time-averaged velocity along the z-axis ($\overline{V_z}/\Omega R$) and velocity profiles extracted at z/R = -0.5, 0.7 and 1.5.

In the case of J = 0.1, an overlap of the velocity profiles and a strong similarity between the flow fields are observed almost everywhere in the analyzed flow field. Minor differences can be however observed around x/R = 0.3, probably still due to the presence of the pole which might affect the velocity field in the experimental results. Both at J = 0 and J = 0.1, the velocity near the blade tip is accurately captured by the URANS simulations, indicating that the tip vortex is well computed. In the URANS simulations, there is finally an additional relevant vortical structure at the root of the blades, due to the cutting of the blades at r/R = 0.2 and to the absence of the spinner. This structure evolves downstream carried by the wake like the tip vortex, but features a lower intensity due to the lower tangential velocity of the root sections compared to that those at the tip.

Considering instead the results of the VPM baseline case, an good prediction of the integral values of the loads can be observed, both in hovering and axial inflow. Particularly at J = 0, the relative errors are around -5.0% for $\overline{C_T}$ and +1.4% for $\overline{C_Q}$. The slight underestimation of thrust and overestimation of torque is found again at J = 0.1, where the errors respectively become to -0.4% and +5.1%. Although these errors are small, non-negligible differences are present in the induced velocity field. In the hovering case, the VPM tends to underestimate the wake velocity near the propeller disk, as observable in the velocity profiles extracted at z/R = 0.7. The wake velocity is there averagely lower than the experimental velocity, with about 8% error and it is consequently also lower than the URANS velocity. The wake however appears to be wider in the radial direction, presenting higher axial velocity values for x/R > 0.6 compared to the experimental and the URANS fields. At z/R = 1.5, the wake velocity increases, yet still underestimating the velocity evaluated through the URANS, while almost overlapping the experimental velocity profile. Locally, the wake evaluated through the VPM expands more towards x/R = 0. The velocity in this area is greater than in the URANS case, which does not expand in the radial direction up to the rotation axis. This separation from the rotation axis is less evident in the VPM simulations. A further difference is observable near the tip and root of the blade. The negative velocity induced by the presence of the tip vortex is lower in absolute value, indicating that the intensity of this vortex might be

underestimated by the VPM code. On the contrary, at the blade root, a more extended zone with greater velocity in absolute value can be observed compared to the URANS case, indicating that the root vortex might have been instead overestimated.

In the case of axial inflow at $J = 0.1$, despite the integral values of $\overline{C_T}$ and $\overline{C_Q}$ are close to the experimental and the URANS values, the axial velocity field displays non-negligible differences. The axial velocity is generally lower compared to the other two methodologies with errors around 5-6% in the core of the wake both at $z/R = 0.7$ and $z/R = 1.5$. However, the wake simulated by the VPM appears wider in the radial direction, displaying higher velocity values with respect to experiments and the URANS between $x/R > 0.6$ and $x/R < 0.9$. Unlike the hovering case, in the region close to the propeller's rotation axis, the velocity profiles of the VPM case overlap with those extracted from the URANS simulations. The presence of the spinner thus seems to be relevant for the axial velocity field especially at low J, while at significant axial inflow velocities this effect appears to be reduced.

To conclude the comparison, the VPM is characterized by a significantly reduced computational cost compared to URANS simulations. A single revolution in hovering is averagely simulated by VULCAINS in a CPU time of about 7.6% the time needed in the URANS computations. In the case of axial inflow, the computational cost per CPU is further reduced, reaching approximately the 4.8% relatively to the URANS.

B. Influence of the input parameters

The study of the influence of the input parameters is initially conducted by evaluating the relative error $\delta(\cdot)$ of some relevant scalar ($\overline{C_T}$, $\overline{C_Q}$, σ_{C_T} and C_{CPU}) and 1D quantities ($\overline{s_{C_T}}$ and $\overline{V_z}/\Omega R$) with respect to the baseline case. In tables 3 and 4 the values of $\delta(\cdot)$ obtained for each of the analyzed cases are displayed. The input parameters corresponding to the baseline case are highlighted in bold.

Table 3 Relative deviation δ with respect to the baseline case quantities. Influence of the number of sources (N_S), the azimuthal angle swept per time-step ($\Delta\psi$) and the integration order.

		N_S					$\Delta\psi$ [°]			Integration Order			
J	$\delta(\cdot)$ [%]	20	30	**40**	50	60	2.5	**5**	10	1	2	**3**	4
0.0	$\overline{C_T}$	-1.2	+0.0	-	-0.1	-3.4	+0.0	-	+0.6	-1.4	+0.1	-	-0.2
	$\overline{C_Q}$	-3.7	-0.9	-	+0.1	-2.4	+0.0	-	+0.3	-1.4	+0.2	-	-0.5
	σ_{C_T}	-37.0	-62.0	-	+67.8	+173.0	+4.1	-	+17.3	+9.5	+12.6	-	+5.3
	$\overline{s_{C_T}}$	3.4	1.4	-	1.3	4.0	0.3	-	1.2	1.1	0.1	-	0.4
	$\overline{V_z}/\Omega R$	12.5	9.4	-	6.9	21.7	0.8	-	2.3	5.7	0.7	-	3.2
	C_{CPU}	-62.2	-29.1	-	+47.6	+117.0	+113.0	-	-51.7	-48.3	-25.7	-	+34.9
0.1	$\overline{C_T}$	+0.2	+0.0	-	+0.1	+0.1	-0.1	-	+0.5	-0.3	+0.0	-	+0.1
	$\overline{C_Q}$	-0.4	-0.2	-	+0.2	+0.3	+0.0	-	+0.1	-0.1	+0.0	-	+0.0
	σ_{C_T}	-15.3	-3.5	-	+11.8	+21.7	+10.0	-	-13.0	-12.2	+4.7	-	-17.0
	$\overline{s_{C_T}}$	3.3	1.5	-	1.2	1.8	0.6	-	1.3	0.2	0.0	-	0.1
	$\overline{V_z}/\Omega R$	9.8	3.0	-	1.8	2.8	0.5	-	1.8	0.5	0.0	-	0.7
	C_{CPU}	-66.8	-39.1	-	+42.2	+102.0	+109.0	-	-44.9	-44.8	-22.7	-	+21.2

1. Number of sources (N_S)

The influence of N_S is more significant in hovering with respect to the axial inflow case, where generally lower $\delta(\cdot)$ values are obtained. Regarding the impact on the time-averaged loads, the relative errors are not negligible but do not exceed in absolute value 3.4% for thrust and 3.7% for torque in hovering. Focusing on σ_{C_T}, an increasing trend can be observed with the increase of N_S. At $N_S = 60$ particles, σ_{C_T} increases by +173% with respect to the baseline case. It's necessary however to highlight that in the baseline case, σ_{C_T} is about 0.4% of $\overline{C_T}$; consequently, even such a significant increase leads to a small value of $\sigma_{C_T}/\overline{C_T}$.

Table 4 Relative deviation δ with respect to the baseline case quantities. Influence of the diffusion scheme, the turbulent viscosity model and the enstrophy filter cutoff frequency (f_0).

		Diffusion Scheme			Turbulent Viscosity Model			f_0		
J	$\delta(\cdot)$ [%]	PSE	**DVM**	CSM	Mansour	**Vreman**	Smargorinsky	0.25	**0.75**	1.25
0.0	$\overline{C_T}$	+0.0	-	0.2	+0.2	-	-0.5	+0.5	-	-0.3
	$\overline{C_Q}$	-0.2	-	-0.1	+0.2	-	-0.5	+0.9	-	-0.5
	σ_{C_T}	+23.7	-	-35.3	+13.3	-	+22.6	+95.4	-	-29.3
	$\overline{s_{C_T}}$	0.5	-	0.45	0.2	-	0.6	0.7	-	0.4
	$\overline{V_z}/\Omega R$	2.4	-	1.7	0.7	-	1.8	3.9	-	2.1
	C_{CPU}	+95.6	-	+13.9	-5.5	-	+6.4	-11.6	-	+11.4
0.1	$\overline{C_T}$	+0.2	-	-0.1	+0.0	-	+0.1	-0.1	-	+0.1
	$\overline{C_Q}$	+0.1	-	+0.0	+0.0	-	+0.0	+0.0	-	+0.0
	σ_{C_T}	-12.7	-	+18.0	+3.1	-	-12.4	+19.2	-	-13.5
	$\overline{s_{C_T}}$	0.2	-	0.1	0.0	-	0.1	0.2	-	0.1
	$\overline{V_z}/\Omega R$	1.5	-	0.7	0.2	-	0.8	1.3	-	0.7
	C_{CPU}	+8.6	-	-5.35	-0.4	-	-0.2	-1.8	-	+0.4

The C_T time histories of the different cases are displayed in figure 5 and it can be noted that the amplitude of the high-frequency C_T oscillations increases with the number of sources, likely due to the numerous interactions between the lifting lines and the growing number of surrounding particles at each iteration. At $N_S = 50$ and 60, lower frequency oscillations around the time-averaged value are also noticeable, while they were less visible or practically negligible at lower N_S values. Finally, although C_T converges to slightly different values, this convergence is reached approximately after 30 revolutions at the largest N_S value. In figure 5, the C_T time histories in the case of axial inflow are also displayed. Under these operating conditions, the time-averaged value is almost identical across the various N_S values, with errors in absolute value below 0.4%. C_T converges in all cases after approximately 10 revolutions, presenting a $\sigma_{C_T}/\overline{C_T}$ around 3.16e-5, which, despite again appearing to increase with N_S, remains small and almost negligible even at $N_S = 60$.

Analyzing the $\delta\overline{s_{C_T}}$ values, non-negligible values are obtained for $N_S = 20$ and 60. In figure 6, the sectional thrust distributions are shown and they almost overlap up to about $r/R = 0.8$, then showing some differences near the tip at r/R close to 1. At $J = 0$, the sectional thrust obtained for $N_S = 60$ appears to slightly underestimate the one obtained at lower N_S values, while more significant differences towards the tip are observable also among all the remaining cases. The higher the N_S value, the more the load towards the tip appears underestimated. This aspect also occurs in axial inflow. Such peculiarity in the tip region is typical of potential methods which see strong positive thrust gradients due to the tip vortex induction and due to the methods' intrinsic inability of capturing the virtual camber effect. For this purpose, specific analytical correction functions have been implemented in other solvers, managing to improve the loads computation close to the blades tip [51]. This effect is indeed not present in higher-fidelity simulations as URANS or LES, where the thrust and torque peak is recorded between 60 and 80% of the radius with a monotonically decreasing trend towards the tip. Another fundamental aspect to evaluate is the influence of N_S on the axial velocity in the wake. The variation of N_S results in the highest $\delta\overline{V_z}/\Omega R$, reaching values as high as 21.7% at $N_S = 60$ in hovering and 9.8% for $N_S = 20$ in axial inflow. In figure 7, the velocity profiles extracted at $z/R = 1$ for the different N_S values are displayed. In hovering, the greatest differences are observed especially in the wake core (approximately between $x/R > 0.3$ and $x/R < 0.6$). As N_S increases, a trend of increasing $\overline{V_z}/\Omega R$ is observed in this area. The $N_S = 60$ case stands out, showing a strong increase both in the core and in the inner zone towards $x/R = 0$. In this latter area, the greatest differences are concentrated for the axial inflow operative condition at $J = 0.1$. The differences between the profiles are indeed exclusively confined to $x/R < 0.3$, while, in the wake core, the profiles are almost overlapped. In conclusion, an additional trend can be observed for what regards the computational cost. The computational cost per core C_{CPU} appears to increase with the number of particles in both hovering and axial inflow. At $N_S = 60$, C_{CPU} is almost doubled for both the J values.

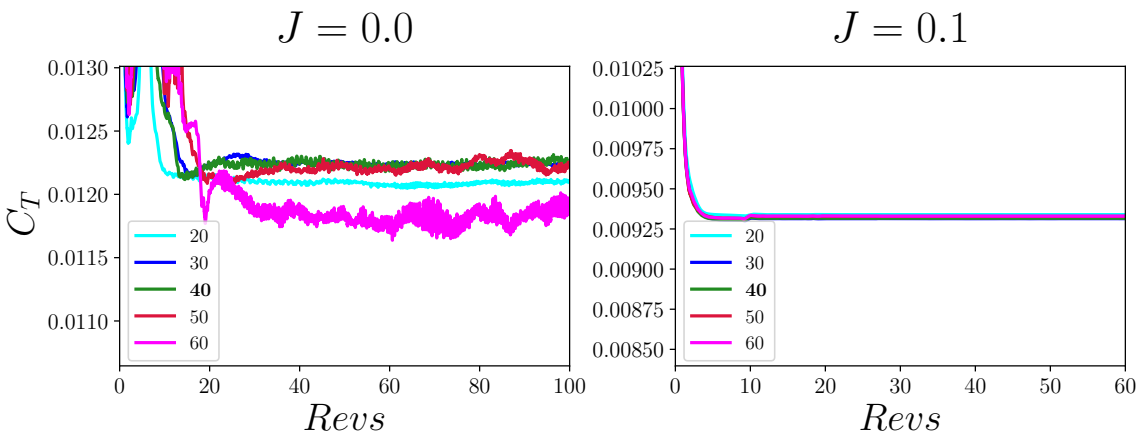

Fig. 5 Time-histories of C_T for the different values of N_s.

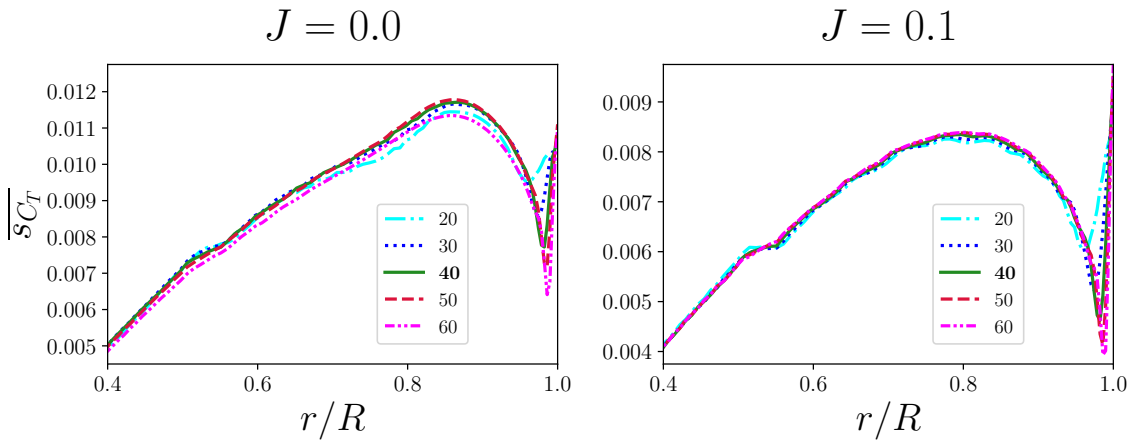

Fig. 6 Sectional non-dimensional thrust $\overline{s_{C_T}}$ along r/R for the different values of N_s.

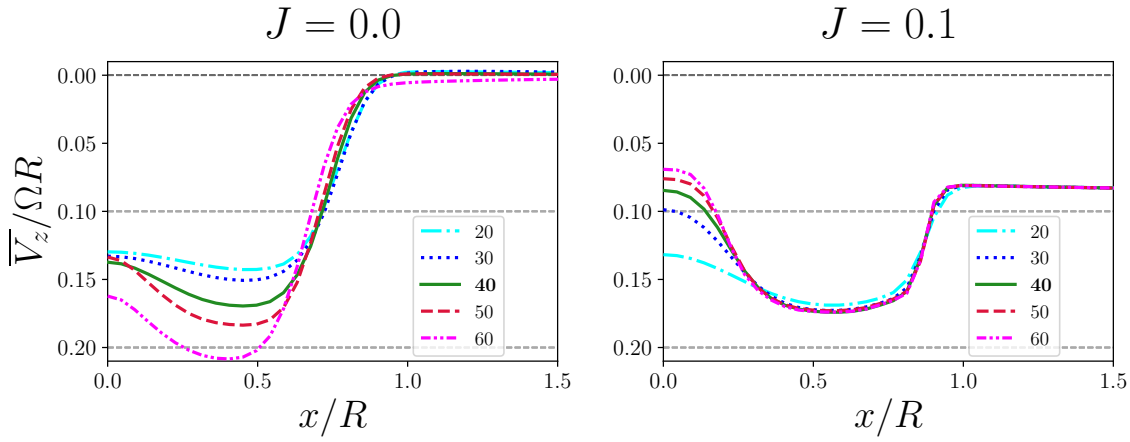

Fig. 7 Non-dimensional axial velocity $\overline{V_z}/\Omega R$ profile extracted at z/R = 1 for the different values of N_s.

2. Discretization in the azimuthal direction ($\Delta\psi$)

The azimuthal angle swept per iteration ($\Delta\psi$) shows an almost negligible influence on the analyzed quantities. Both in hovering and axial inflow, errors in average loads are lower than 0.6%, and no significant variations are observed in σ_{C_T}. The only remarkable effect of the $\Delta\psi$ increasing to 10° is a slight reduction in the wake velocity for $x/R < 0.3$, being however almost negligible if compared to what observed for N_S. Nevertheless, it is expected that a much higher $\Delta\psi$ might significantly influence the final solution, even though $\Delta\psi > 10°$ is almost never taken into account in the numerical simulation of rotating lifting lines. Finally, the only significant effect of increasing $\Delta\psi$ is to decrease C_{CPU} by about 50% when moving from 5° to 10°, and to increase it by about 100% when reducing $\Delta\psi$ from 5 to 2.5°.

3. Order of Integration in Time

The choice of the order of integration in time does not impact the final solution as significantly as N_S. In particular, the average loads are not affected beyond 1.4% in hovering and 0.3% in axial inflow and σ_{C_T} is not particularly impacted either. However, observing the C_T time histories at $J = 0$ in figure 8, the choice of a 1^{st} order integration scheme leads to a C_T trend which is initially very similar to the 2^{nd} and 3^{rd} order trends, but C_T seems to slightly diverge from the average solution calculated for higher orders as the simulation advances. For what instead concerns the 4^{th} order, the solution reaches convergence only around the 40^{th} revolution, displaying strong oscillations in the previous iterations, not present in lower orders time histories. Almost negligible differences are instead present in the wake velocity profile. The choice of a higher integration order ensures better accuracy of the solution over time, but it comes with some disadvantages, including an increased computational cost. However, this increase is limited with respect to what observed for small $\Delta\psi$ or high N_S.

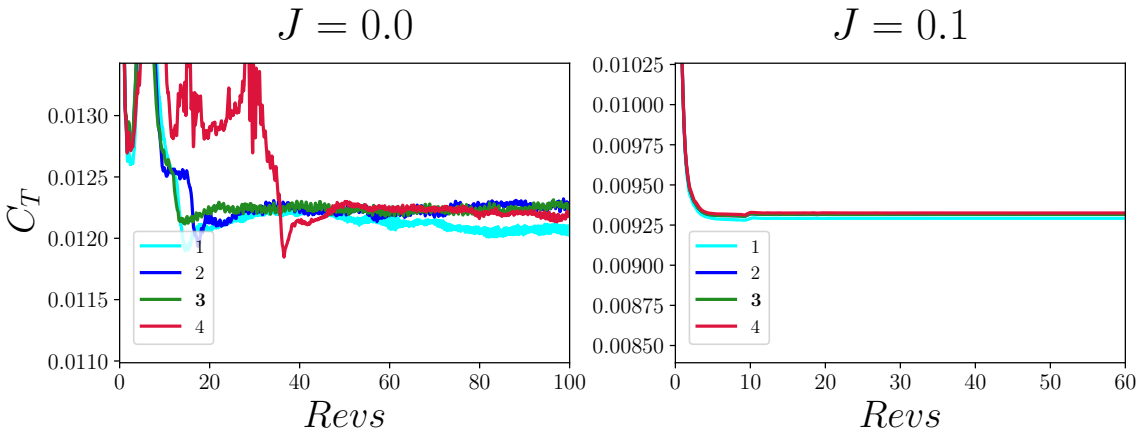

Fig. 8 Time-histories of C_T for the different orders of integration.

4. Diffusion Scheme

The choice of the diffusion scheme is almost negligible in terms how it affects the time-averaged loads and wake velocity, with particularly the velocity profiles being almost overlapped. However, by observing the C_T time histories in hovering as reported in figure 9, an unexpected trend of the CSM solution is observed. The solution significantly oscillates above the mean value until almost the 60^{th} revolution, however ultimately converging to a mean value which is very close to the other schemes. This behavior makes the numerical scheme unreliable, especially because the simulations are typically run for fewer revolutions to save on computational cost. Regarding the computational cost, C_{CPU} increases by only +13.9% in hovering for the CSM scheme, while it increases by up to +95.6% for the PSE scheme, making the latter less advantageous due to the frequent required particle distribution in the domain.

5. Turbulent Viscosity Model

The turbulence viscosity model does not appear to have a significant influence on the solution, neither in terms of loads nor wake velocity. Moreover, it does not seem to have a significant impact on the computational time either, which

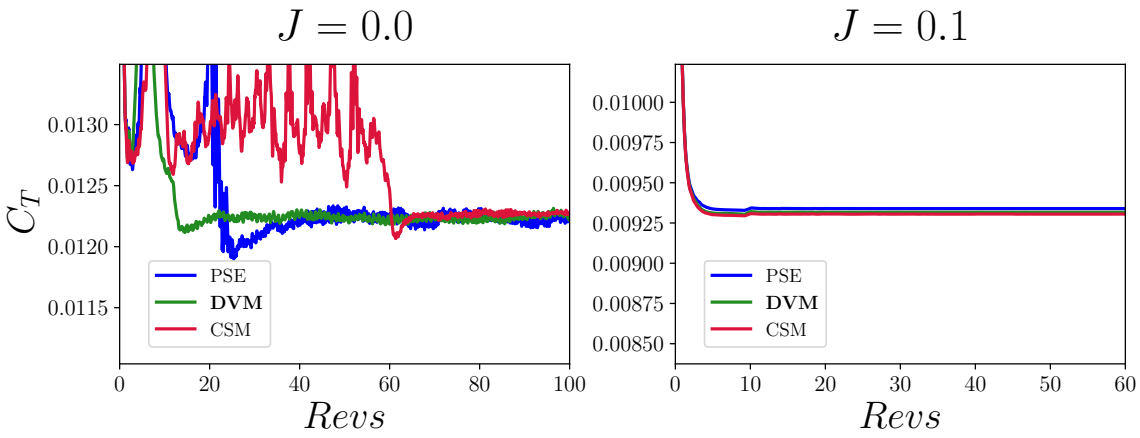

Fig. 9 Time-histories of C_T for the different considered diffusion schemes.

varies at most by +6.4% for the Smargorinsky model in the hovering conditions.

6. Enstrophy filter cutoff frequency (f_0)

The last investigated parameter is the enstrophy filter cutoff frequency f_0, which determines the intensity of the filter to control the particles' strength in magnitude and orientation. A higher value of this parameter indicates a greater filter intensity, often useful in highly turbulent flows to maintain a divergence-free velocity field. The effect of f_0 appears to be almost negligible in both hovering and axial inflow conditions regarding average loads and load distribution along the blade. The σ_{C_T} is reduced with the increase of f_0; however, as observable in figure 10 at $J = 0$, the case with $f_0 = 1.25$ requires more revolutions to reach convergence. On the other hand in axial inflow condition, negligible difference are instead observable among the different C_T time histories. Choosing an f_0 different from the baseline also leads to slight differences in velocity profiles, as observable in 11. In hovering, an increase of f_0 results in a decrease of the axial velocity in the wake core, while it has a negligible effect in the case of axial inflow. To conclude, no significant effect is instead observed in the computational cost of the simulations.

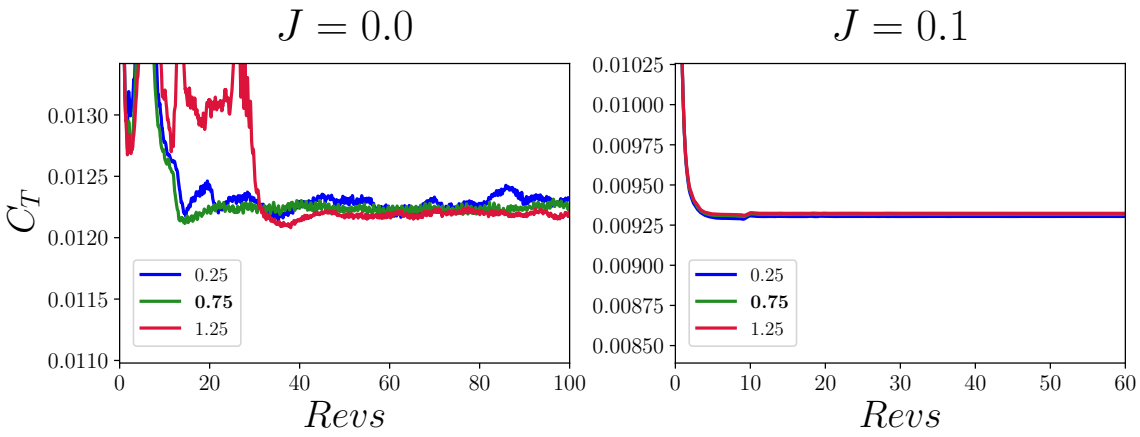

Fig. 10 Time-histories of C_T for the different values of the cutoff frequency f_0.

VI. Conclusions

In the present work, a multi-fidelity analysis was conducted on a small drone propeller, aiming to compare the VPM code VULCAINS with higher fidelity methodologies such as URANS and experiments. The propeller was investigated

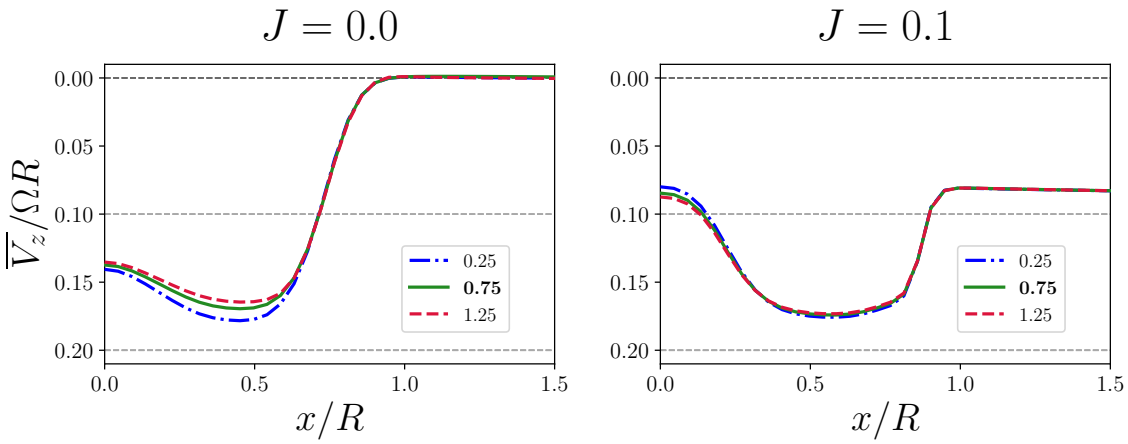

Fig. 11 Non-dimensional axial velocity $\overline{V_z}/\Omega R$ profile extracted at z/R = 1 for the different values of the cutoff frequency f_0.

in hovering and axial inflow conditions, focusing on its performance in terms of thrust and torque, and on the induced wake in terms of axial velocity. The three methodologies yielded similar results, especially for the axial inflow case, where relative thrust and torque differences with respect to the experimental results were under 4% for both the URANS and VPM results. However, the URANS better predicts the axial velocity in the wake, overlapping with experimental data in almost the entire investigated area except close to the rotation axis, where slight errors are observed due to the absence of the spinner in the numerical simulations. The VPM instead underestimates the axial velocity in the wake core with errors around 5%.

In the hovering case, the differences are instead more pronounced among the three methodologies. The errors in thrust and torque coefficients reach up to 8%, while the axial velocity in the wake is overestimated by the URANS with errors between 8% and 15% and underestimated by the VPM with errors around 5%, especially close to the propeller disk. Moreover, a maximum velocity region is detected around half a radius distance in the axial direction in the experimental results, while in the URANS and VPM results, the velocity is observed to increase at least up to 1.5 radii of distance from the propeller disk. This difference in flow field may again be due to the absence of the spinner in numerical simulations.

Subsequently, an investigation was conducted on the influence of the VPM input parameters on the results. Among the analyzed parameters, the number of vorticity sources shed by the blades per time step proved to be the most influential. Compared to the baseline value of 40 particles, the maximum difference is obtained by increasing the number of particles to 60. While thrust and torque coefficients vary around 3% in hovering and 0.2% in axial inflow, the greatest differences are obtained in hovering in the wake velocity magnitude, which increases by around 15% in its core. The axial velocity indeed appears to increase with the increase of the number of particles. The computational cost also increases with the number of particles, doubling from 40 to 60 particles. Other analyzed input parameters did not show a substantial influence as the number of vorticity sources. However, focusing on thrust time histories in some specific cases, it was observed that many propeller revolutions were sometimes required before reaching convergence. The use of the CSM diffusion scheme is the most representative example, where more than 60 revolutions are needed to reach the loads convergence in hovering, while 20 revolutions were sufficient in the baseline case using the DVM diffusion scheme.

The analysis carried out has allowed to assess the accuracy and the advantages of the VPM code VULCAINS in simulating a small drone propeller in hovering and axial inflow. The VPM code, characterized by ease of setup and low computational cost, results to be an optimal tool especially for the preliminary design phases. The limited influence of the investigated input parameters ensures that these parameters do not necessarily need to be calibrated for each individual test case, although certain choices might lead to a solution which is more similar to higher fidelity solutions. A critical parameter not analyzed in this work is the choice of aerodynamic polars, which are not straightforward to be computed at these low Reynolds numbers. The choice of using XFoil has led to overall good results, but it was calibrated by comparing the final VPM results

The choice of XFoil polars has led to an overall good prediction of the loads and velocity fields in comparison with

experimental and URANS results. Nevertheless, the choice of the N_{cr} value was not straightforward at the analyzed low Reynolds numbers, since its value significantly influences the final results.

As a future outlook, the aim is to investigate the influence of the aerodynamic polars and to simulate the spinner in the URANS simulations, to observe its influence on the flow field.

Funding Sources

This work is part of the project PNRR-NGEU which has received funding from the MUR-DM352/2022. This study was carried out within the MOST – Sustainable Mobility National Research Center and received funding from the European Union Next-GenerationEU (PIANO NAZIONALE DI RIPRESA E RESILIENZA (PNRR) – MISSIONE 4 COMPONENTE 2, INVESTIMENTO 1.4 – D.D. 1033 17/06/2022, CN00000023). This manuscript reflects only the authors' views and opinions, neither the European Union nor the European Commission can be considered responsible for them.

Acknowledgments

G. A. acknowledges ONERA for co-sponsoring the PhD studentship. The authors acknowledge Johan Valentin for his support on the use of the VULCAINS code and for his precious help on the interpretation of the results. The authors finally acknowledge the members of the team EoliTo for the use of the 3D printer.

References

[1] Moradi, N., Wang, C., and Mafakheri, F., "Urban Air Mobility for Last-Mile Transportation: A Review," *Vehicles*, Vol. 6, No. 3, 2024, pp. 1383–1414. https://doi.org/https://doi.org/10.3390/vehicles6030066.

[2] Sauls, L. A., Paneque-Gálvez, J., Amador-Jiménez, M., Vargas-Ramírez, N., and Laumonier, Y., "Drones, communities and nature: pitfalls and possibilities for conservation and territorial rights," *Global Social Challenges Journal*, Vol. 2, No. 1, 2023, pp. 24–46. https://doi.org/https://doi.org/10.1332/AJHA9183.

[3] Puri, V., Nayyar, A., and Raja, L., "Agriculture drones: A modern breakthrough in precision agriculture," *Journal of Statistics and Management Systems*, Vol. 20, No. 4, 2017, pp. 507–518. https://doi.org/https://doi.org/10.1080/09720510.2017.1395171.

[4] Gargalakos, M., "The role of unmanned aerial vehicles in military communications: application scenarios, current trends, and beyond," *The Journal of Defense Modeling and Simulation*, Vol. 21, No. 3, 2024, pp. 313–321. https://doi.org/https://doi.org/10.1177/15485129211031668.

[5] Analytica, A., "Unmanned Aerial Vehicle (UAV) Market Valuation Skyrocketing to Reach US$ 119.71 Billion By 2032," Tech. rep., Astute Analytica, 2023. URL https://www.astuteanalytica.com/industry-report/unmanned-aerial-vehicle-market.

[6] Grava, A., Jacopo, S., Gaetano, I., Luis, B., and Gioacchino, C., "Experimental Investigation of a Small Drone Propeller Aerodynamics in Forward Flight," *AIAA Journal*, 2024, pp. 1–12. https://doi.org/https://doi.org/10.2514/1.J064664.

[7] Carreño Ruiz, M., Scanavino, M., D'Ambrosio, D., Guglieri, G., and Vilardi, A., "Experimental and numerical analysis of hovering multicopter performance in low-Reynolds number conditions," *Aerospace Science and Technology*, Vol. 128, 2022, p. 107777. https://doi.org/https://doi.org/10.1016/j.ast.2022.107777, URL https://www.sciencedirect.com/science/article/pii/S1270963822004515.

[8] Pérez Gordillo, A. M., Escobar, J. A., and Lopez Mejia, O. D., "Influence of the Reynolds Number on the Aerodynamic Performance of a Small Rotor," *Aerospace*, Vol. 10, No. 2, 2023, p. 130. https://doi.org/https://doi.org/10.3390/aerospace10020130.

[9] Liu, X., Zhao, D., and Oo, N. L., "Comparison studies on aerodynamic performances of a rotating propeller for small-size UAVs," *Aerospace Science and Technology*, Vol. 133, 2023, p. 108148. https://doi.org/https://doi.org/10.1016/j.ast.2023.108148.

[10] Cerny, M., and Breitsamter, C., "Investigation of small-scale propellers under non-axial inflow conditions," *Aerospace Science and Technology*, Vol. 106, 2020, p. 106048. https://doi.org/https://doi.org/10.1016/j.ast.2020.106048.

[11] Milluzzo, J., and Leishman, J. G., "Fluid dynamics of the helicoidal wake sheets trailed from a hovering rotor," *Journal of the American Helicopter Society*, Vol. 61, No. 1, 2016, pp. 1–17. https://doi.org/https://doi.org/10.4050/JAHS.61.012002.

[12] Yang, Y., Liu, Y., Li, Y., Arcondoulis, E., and Wang, Y., "Aerodynamic and aeroacoustic performance of an isolated multicopter rotor during forward flight," *AIAA Journal*, Vol. 58, No. 3, 2020, pp. 1171–1181. https://doi.org/https://doi.org/10.2514/1.J058459.

[13] Winslow, J., Otsuka, H., Govindarajan, B., and Chopra, I., "Basic understanding of airfoil characteristics at low Reynolds numbers (10 4–10 5)," *Journal of aircraft*, Vol. 55, No. 3, 2018, pp. 1050–1061. https://doi.org/https://doi.org/10.2514/1.C034415.

[14] Wang, S., Zhou, Y., Alam, M. M., and Yang, H., "Turbulent intensity and Reynolds number effects on an airfoil at low Reynolds numbers," *Physics of Fluids*, Vol. 26, No. 11, 2014. https://doi.org/https://doi.org/10.1063/1.4901969.

[15] Menter, F. R., "Two-equation eddy-viscosity turbulence models for engineering applications," *AIAA journal*, Vol. 32, No. 8, 1994, pp. 1598–1605. https://doi.org/https://doi.org/10.2514/3.12149.

[16] Menter, F. R., Langtry, R., and Völker, S., "Transition modelling for general purpose CFD codes," *Flow, turbulence and combustion*, Vol. 77, 2006, pp. 277–303. https://doi.org/https://doi.org/10.1007/s10494-006-9047.

[17] Valentin, J., and Bernardos, L., "Validation of a new solver based on the vortex particle method for wings, propellers and rotors," *ERF-European Rotorcraft Forum 2023*, 2023.

[18] Valentin, J., Bernardos, L. F., Pinon, G., and Rivoalen, E., "Hybrid Eulerian-Lagrangian Method for Complex 3D Viscous Flows," *AIAA AVIATION FORUM AND ASCEND 2024*, 2024, p. 3865. https://doi.org/https://doi.org/10.2514/6.2024-3865.

[19] Valentin, J., "Multi-Fidelity Coupling of Vortex Particles with Lifting Lines and Eulerian Methods for the Simulation of 3D Viscous Aeronautical Flows," Ph.D. thesis, École Doctorale Physique, Sciences de l'Ingénieur, Matériaux, Énergie, INSA Rouen Normandie, 2024.

[20] Singh, P., and Friedmann, P. P., "Application of vortex methods to coaxial rotor wake and load calculations in hover," *Journal of Aircraft*, Vol. 55, No. 1, 2018, pp. 373–381. https://doi.org/https://doi.org/10.2514/1.C034520.

[21] Alvarez, E. J., and Ning, A., "Modeling multirotor aerodynamic interactions through the vortex particle method," *AIAA Aviation 2019 Forum*, 2019, p. 2827. https://doi.org/https://doi.org/10.2514/6.2019-2827.

[22] Lee, H., and Lee, D.-J., "Numerical investigation of the aerodynamics and wake structures of horizontal axis wind turbines by using nonlinear vortex lattice method," *Renewable Energy*, Vol. 132, 2019, pp. 1121–1133. https://doi.org/https://doi.org/10.1016/j.renene.2018.08.087, URL https://www.sciencedirect.com/science/article/pii/S0960148118310371.

[23] Stock, M., Gharakhani, A., and Stone, C., "Modeling rotor wakes with a hybrid OVERFLOW-vortex method on a GPU cluster," *28th AIAA applied aerodynamics conference*, 2010, p. 4553. https://doi.org/https://doi.org/10.2514/6.2010-4553.

[24] Chatelain, P., Duponcheel, M., Caprace, D.-G., Marichal, Y., and Winckelmans, G., "Vortex particle-mesh simulations of vertical axis wind turbine flows: from the airfoil performance to the very far wake," *Wind Energy Science*, Vol. 2, No. 1, 2017, pp. 317–328. https://doi.org/https://doi.org/10.5194/wes-2-317-2017.

[25] Tan, J., Sun, Y., and Barakos, G., "Unsteady loads for coaxial rotors in forward flight computed using a vortex particle method," *The Aeronautical Journal*, Vol. 122, No. 1251, 2018, pp. 693–714. https://doi.org/https://doi.org/10.1017/aer.2018.8.

[26] Drela, M., "XFOIL: An analysis and design system for low Reynolds number airfoils," *Low Reynolds Number Aerodynamics: Proceedings of the Conference Notre Dame, Indiana, USA, 5–7 June 1989*, Springer, 1989, pp. 1–12.

[27] Lee, K.-H., Jeon, Y.-H., Kim, K.-H., Lee, D.-H., and Lee, K.-T., "Three-Dimensional Micro Propeller Design by Using Efficient Two Step Optimization," *Journal of Fluid Science and Technology*, Vol. 2, No. 2, 2007, pp. 334–345. https://doi.org/https://doi.org/10.1299/jfst.2.334.

[28] Gunel, O., Koç, E., and Yavuz, T., "Comparison of CFD and Xfoil airfoil analyses for low Reynolds number," *International Journal of Energy Applications and Technologies*, Vol. 3, No. 2, 2016, pp. 83–86.

[29] Morgado, J., Vizinho, R., Silvestre, M., and Páscoa, J., "XFOIL vs CFD performance predictions for high lift low Reynolds number airfoils," *Aerospace Science and Technology*, Vol. 52, 2016, pp. 207–214. https://doi.org/https://doi.org/10.1016/j.ast.2016.02.031.

[30] Plante, F., Dandois, J., Beneddine, S., Laurendeau, É., and Sipp, D., "Link between subsonic stall and transonic buffet on swept and unswept wings: from global stability analysis to nonlinear dynamics," *Journal of Fluid Mechanics*, Vol. 908, 2021, p. A16. https://doi.org/https://doi.org/10.1017/jfm.2020.848.

[31] Mansfield, J. R., Knio, O. M., and Meneveau, C., "Dynamic LES of colliding vortex rings using a 3D vortex method," *Journal of Computational Physics*, Vol. 152, No. 1, 1999, pp. 305–345. https://doi.org/https://doi.org/10.1006/jcph.1999.6258.

[32] Mansfield, J. R., Knio, O. M., and Meneveau, C., "A dynamic les scheme for the vorticity transport equation: Formulation anda prioritests," *Journal of Computational Physics*, Vol. 145, No. 2, 1998, pp. 693–730.

[33] Wang, T., Yokota, R., and Barba, L. A., "ExaFMM: a high-performance fast multipole method library with C++ and Python interfaces," *Journal of Open Source Software*, Vol. 6, No. 61, 2021, p. 3145. https://doi.org/https://doi.org/10.21105/joss.03145.

[34] Leonard, A., "Vortex methods for flow simulation," *journal of computational physics*, Vol. 37, No. 3, 1980, pp. 289–335. https://doi.org/https://doi.org/10.1016/0021-9991(80)90040-6.

[35] Mas-Gallic, S., "Contribution à l'analyse numérique des méthodes particulaires," Ph.D. thesis, Paris 6, 1987.

[36] Mycek, P., Pinon, G., Germain, G., and Rivoalen, É., "A self-regularising DVM–PSE method for the modelling of diffusion in particle methods," *Comptes Rendus Mécanique*, Vol. 341, No. 9-10, 2013, pp. 709–714. https://doi.org/https://doi.org/10.1016/j.crme.2013.08.002.

[37] Mycek, P., Pinon, G., Germain, G., and Rivoalen, E., "Formulation and analysis of a diffusion-velocity particle model for transport-dispersion equations," *Computational and Applied Mathematics*, Vol. 35, 2016, pp. 447–473. https://doi.org/https://doi.org/10.1007/s40314-014-0200-5.

[38] Mas-Gallic, S., "The diffusion velocity method: a deterministic way of moving the nodes for solving diffusion equations," *Transport Theory and Statistical Physics*, Vol. 31, No. 4-6, 2002, pp. 595–605.

[39] Yokota, R., Barba, L. A., Narumi, T., and Yasuoka, K., "Petascale turbulence simulation using a highly parallel fast multipole method on GPUs," *Computer Physics Communications*, Vol. 184, No. 3, 2013, pp. 445–455. https://doi.org/https://doi.org/10.1016/j.cpc.2012.09.011.

[40] Tollmien, W., Schlichting, H., Görtler, H., Tollmien, W., Schlichting, H., Görtler, H., and Riegels, F., "Bericht über Untersuchungen zur ausgebildeten Turbulenz," *Ludwig Prandtl Gesammelte Abhandlungen: zur angewandten Mechanik, Hydro-und Aerodynamik*, 1961, pp. 714–718.

[41] Smargorinsky, J., "General circulation experiment with the primitive equations," *Monthly Weather Review*, Vol. 91, No. 3, 1963, pp. 99–164. https://doi.org/http://dx.doi.org/10.1175/1520-0493(1963)091<0099:GCEWTP>2.3.CO;2.

[42] Kwak, D., Reynolds, W. C., and Ferziger, J. H., "Three-dimensional time dependent computation of turbulent flow," Tech. rep., 1975.

[43] Vreman, A., "An eddy-viscosity subgrid-scale model for turbulent shear flow: Algebraic theory and applications," *Physics of fluids*, Vol. 16, No. 10, 2004, pp. 3670–3681. https://doi.org/https://doi.org/10.1063/1.1785131.

[44] Pedrizzetti, G., "Insight into singular vortex flows," *Fluid Dynamics Research*, Vol. 10, No. 2, 1992, p. 101. https://doi.org/https://doi.org/10.1016/0169-5983(92)90011-K.

[45] Grava, A., Picillo, M., Serpieri, J., Iuso, G., Bernardos, L., and Cafiero, G., "Aerodynamic investigation of a drone propeller in cross-flow," *AIAA SCITECH 2024 Forum*, 2024, p. 0244. https://doi.org/https://doi.org/10.2514/6.2024-0244.

[46] Casalino, D., Grande, E., Romani, G., Ragni, D., and Avallone, F., "Definition of a benchmark for low Reynolds number propeller aeroacoustics," *Aerospace Science and Technology*, Vol. 113, 2021, p. 106707. https://doi.org/https://doi.org/10.1016/j.ast.2021.106707.

[47] Cambier, L., Heib, S., and Plot, S., "The Onera elsA CFD software: input from research and feedback from industry," *Mechanics & Industry*, Vol. 14, No. 3, 2013, pp. 159–174. https://doi.org/https://doi.org/10.1051/meca/2013056.

[48] Webster, J., Neu, W., and Brizzolara, S., "Reynolds stress transition modeling for marine propellers at low Reynolds number," *Sixth International Symposium on Marine Propulsors: Smp19*, 2019.

[49] Loureiro, E. V., Oliveira, N. L., Hallak, P. H., de Souza Bastos, F., Rocha, L. M., Delmonte, R. G. P., and de Castro Lemonge, A. C., "Evaluation of low fidelity and CFD methods for the aerodynamic performance of a small propeller," *Aerospace Science and Technology*, Vol. 108, 2021, p. 106402. https://doi.org/https://doi.org/10.1016/j.ast.2020.106402.

[50] Critzos, C. C., Heyson, H. H., and Boswinkle Jr, R. W., "Aerodynamic characteristics of NACA 0012 airfoil section at angles of attack from 0 deg to 180 deg," *Report No. NASA TN3361*, 1955.

[51] Baars, W. J., Dacome, G., and Lee, M., "Reynolds-number scaling of wall-pressure–velocity correlations in wall-bounded turbulence," *Journal of Fluid Mechanics*, Vol. 981, 2024, p. A15. https://doi.org/https://doi.org/10.1017/jfm.2024.46.